Longitudinal System Identification for a Small Flying-Wing UAS

Justin J. Matt*, Haiyang Chao†, and Mosarruf H. Shawon ‡
University of Kansas, Lawrence, KS 66045

Steven G. Hagerott §
Textron eAviation, Wichita, KS 67202

Benjamin C. Svoboda¶
University of Kansas, Lawrence, KS 66045

This paper focuses on identification of the bare-airframe, longitudinal dynamics of a small, flying-wing UAS, including both the short-period and phugoid modes. Servo dynamics from commanded to real control surface deflection angles are first identified, which is important for UAS equipped with low-bandwidth servos. A flight test procedure is developed for longitudinal system identification that includes the collection of trim data, elevator and throttle frequency sweep data, doublet data, and phugoid oscillation data. Throttle and elevator frequency sweep data is used to generate longitudinal frequency responses. Trim data is used to compute the longitudinal speed stability derivatives. Then, a multi-input, multi-output state space model is identified by holding the longitudinal speed stability derivatives constant and fitting the remaining parameters to the measured frequency responses. The identified model is shown to accurately represent the UAS response to elevator deflection and electric motor rotational speed. The identified phugoid mode dynamics show excellent agreement with results obtained from the time-history phugoid oscillation data. Finally, nondimensional stability and control derivatives and their confidence intervals are computed from the identified models.

Nomenclature

IMU	=	inertial measurement unit
LSS	=	longitudinal speed stability
RPM	=	revolutions per minute
TIC	=	Theil inequality coefficient
$\overline{CR}$	=	Cramér-Rao bound percentage
$\bar{I}$	=	insensitivity percentage
J	=	cost function value
X, Z, M	=	longitudinal force, vertical force, and pitching moment stability and control derivatives
U_0, W_0, Θ_0	=	trim x- and z-axis body velocities and trim pitch angle
g	=	gravity constant
n	=	motor speed
q, θ	=	pitch rate and pitch angle
u, w	=	perturbation x- and z-axis body velocities
δ_e^c, δ_a^c	=	elevator and aileron commands
δ_e, δ_a	=	elevator and aileron deflection
$\delta_{\text{left}}, \delta_{\text{right}}$	=	left and right elevon deflection
ζ, ω_n	=	damping coefficient and natural frequency
τ_{δ_e}, τ_n	=	time delay associated with elevator and motor speed inputs

*M.S. Student, Department of Aerospace Engineering, University of Kansas, justinjmatt@gmail.com.
†Associate Professor, Department of Aerospace Engineering, University of Kansas, chaohaiyang@ku.edu.
‡Ph.D. Student, Department of Aerospace Engineering, University of Kansas, mosarruf@ku.edu.
§Principal Engineer, Textron eAviation, shagerott@e-aviation.com.
¶Undergraduate Student, Department of Aerospace Engineering, University of Kansas, ben.svoboda@ku.edu.

I. Introduction

Unmanned aircraft systems (UAS) have become increasingly important platforms for the research and development of next-generation autonomous aircraft, such as urban-air mobility vehicles or autonomous cargo delivery vehicles. A significant step in the development of UAS is the identification of dynamic models, which are critical to many research applications, such as controller design or flight simulation. Frequency domain methods are often used to identify aircraft flight dynamic models from flight data. These techniques have been applied extensively to manned aircraft system identification problems [1, 2]. In recent years, several works have used frequency response-based methods to identify small UAS dynamic models [3–8].

Fully identifying the longitudinal dynamics of a small UAS can be difficult and sometimes unnecessary for certain applications. Modeling of just the short-period dynamics is often sufficient for longitudinal control law design, as the phugoid dynamics are low-frequency and can be compensated for by feedback control. The short-period dynamics are often represented by simplified models that assume a constant forward velocity [5, 7]. However, for other applications, such as flight simulation or comprehensive UAS safety analysis, full quantification of the longitudinal dynamics may be desired. This includes modeling the UAS response to throttle inputs, as was done in [8]. Furthermore, accurate identification of the phugoid mode may require separate experiments from those used for modeling the short-period mode. For example, the longitudinal speed stability (LSS) derivatives of a small UAS, which largely characterize the phugoid mode, were modeled from wind tunnel data rather than flight test data in [4]. For manned aircraft, trim data has been used to determine the LSS derivatives [1, 9].

This paper improves on our previous, frequency response-based system identification work for a small, flying-wing UAS [3]. The identified longitudinal state space model is extended to model the UAS response to both the elevator and propulsion system. The electric motor's rotational speed is measured directly and used as a model input to prevent errors due to nonlinear throttle dynamics caused by the motor input voltage changing over the course of a flight test. Trim data, elevator and throttle frequency sweep data, doublet data, and phugoid oscillation data are collected during flight tests. The throttle and elevator frequency sweep data is used to generate frequency responses, and the trim data is used to identify the LSS derivatives. A multi-input, multi-output state space model is identified by fitting the model to the measured frequency responses, while holding the LSS derivatives constant. Servo dynamics are identified and accounted for during the system identification process. This process is critical for small UAS that are often equipped with low-cost and low-bandwidth servos (e.g., the digital servos herein have a 5 Hz bandwidth), as system identification flight maneuvers may take place at frequencies above the servo bandwidth. Accounting for the servo dynamics ensures that the identified stability derivatives will not be affected by the low servo bandwidth, and, thus, are more comparable with bare-airframe modeling results from other approaches such as wind tunnel tests or CFD simulations. Finally, phugoid mode dynamics are identified from phugoid oscillation time-history data to further validate the obtained results.

This paper is organized as follows. Section II presents the system dynamics and UAS platform used for identification. Section III describes the experimental methods designed for servo model identification, trim data collection for LSS derivative determination, and frequency response system identification. Longitudinal model identification results are presented in Section IV. Section V provides concluding remarks and future directions for this work.

II. Problem Description

A. System Dynamics

The longitudinal dynamics of a UAS are comprised of many different subsystems, including the bare-airframe, servos, and an electric throttle motor, as pictured in Fig. 1. If a single, integrated model is identified to relate the command signals to the UAS response, the model will represent the bare-airframe dynamics and the effects of the servo and motor dynamics. In this paper, the servo and electric motor dynamics are accounted for during the system identification processing, yielding a model that represents solely the bare-airframe dynamics. This section describes the dynamics and models used for each subsystem.

1. Servo Dynamics

Ideally, control surface deflection would be measured directly and used as the control input signal for modeling. For small UAS, however, it is often difficult or impractical to do so due to size and weight constraints. Furthermore, small UAS are often equipped with low-cost servos that may have a bandwidth lower than the operating frequency of flight test maneuvers designed for system identification.

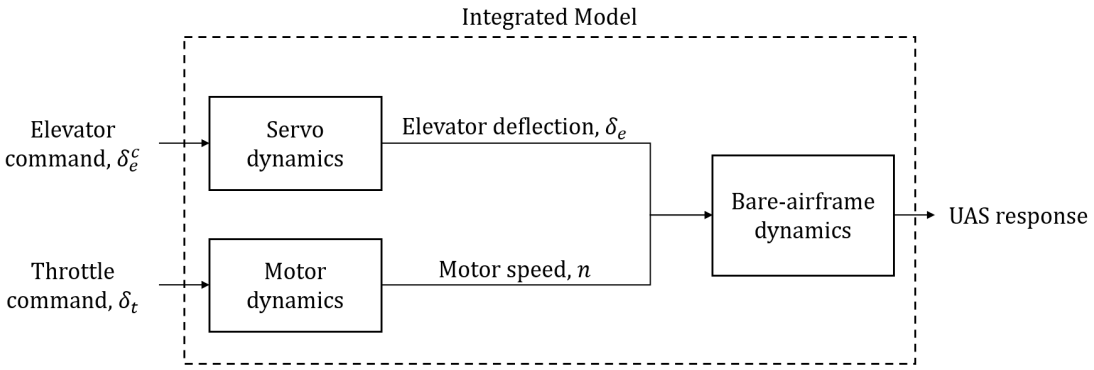

Fig. 1 Longitudinal system diagram.

In this case, the servo dynamics should be determined from ground tests and accounted for in the system identification process. Otherwise, the identified model parameters will be affected by the servo dynamics. This integrated model may be sufficient for certain applications, such as controller design, but may fail to accurately predict the UAS's uncontrolled motion. Consequently, the bare-airframe dynamic modes may be biased, and the identified stability derivatives may not correspond with bare-airframe values identified from other methods such as static wind tunnel testing.

Servo dynamics are often modeled as first- or second-order linear systems. In this paper, a first order structure was found to accurately represent the dynamics:

$$\frac{\delta}{\delta^c} = K_\delta \frac{1}{\tau_{\text{srv}} s + 1} \tag{1}$$

where K_δ is the steady state gain and τ_{srv} is the servo time constant.

2. Propulsion System Dynamics

The propulsion system also has a significant effect on the longitudinal dynamics of a UAS. Often, models are developed from ground-test experiments to predict the thrust produced by the propulsion system at different conditions. For propeller-driven aircraft, the thrust coefficient is commonly modeled as a function of the aircraft advance ratio [10]. The inverse advance ratio was shown to be a good explanatory variable for the dimensional thrust force in [11].

$$J_{\text{adv}} = \frac{V}{nD}, \qquad (J_{\text{adv}})^{-1} = \frac{nD}{V} \tag{2}$$

where V is the UAS airspeed, n is the rotational speed (typically expressed in revolutions per second), and D is the diameter of the propeller.

Linear dynamic models are identified around a certain trim condition and assumed to be valid for relatively small excursions around the trim condition. Under this assumption, $(J_{\text{adv}})^{-1}$ and subsequently the total thrust may be modeled approximately as a linear function of rotational speed. For brushless electric motors, the RPM itself is a function of many factors, including the airspeed, motor voltage, and throttle signal. Because the battery voltage is constantly changing over a flight, the throttle command will be inconsistent even for the same flight conditions. For these reasons, the electric motor RPM was measured directly and used as the an input to the bare-airframe dynamic model, rather than using the throttle signal.

3. Bare-airframe Dynamics

The longitudinal dynamics of fixed-wing aircraft are composed of the short-period and long-period, or phugoid, modes. A simplified set of equations can be constructed to model just the short-period mode by assuming that the forward velocity of the UAS is constant. This assumption is commonly used for pitch controller design, as the phugoid mode is a low-frequency oscillation that can be easily compensated for by feedback. The two degree-of-freedom, short-period dynamics can be written in linear state space form as:

$$\begin{bmatrix} \dot{w} \\ \dot{q} \end{bmatrix} = \begin{bmatrix} Z_w & Z_q \\ M_w & M_q \end{bmatrix} \begin{bmatrix} w \\ q \end{bmatrix} + \begin{bmatrix} Z_{\delta_e} \\ M_{\delta_e} \end{bmatrix} \delta_e(t - \tau_{\delta_e}) \tag{3}$$

where w is the z-axis body velocity, q is the pitch rate, δ_e is the elevator deflection, and τ_{δ_e} is the equivalent elevator time delay that accounts for system delays and data processing.

Similarly, the longitudinal dynamics can be expressed as a three degree-of-freedom system that models both the phugoid and short-period dynamics, linearized about the trim condition. The multi-input model is written as:

$$\begin{bmatrix} \dot{u} \\ \dot{w} \\ \dot{q} \\ \dot{\theta} \end{bmatrix} = \begin{bmatrix} X_u & X_w & X_q - W_0 & -g\cos\Theta_0 \\ Z_u & Z_w & Z_q + U_0 & -g\sin\Theta_0 \\ M_u & M_w & M_q & 0 \\ 0 & 0 & 1 & 0 \end{bmatrix} \begin{bmatrix} u \\ w \\ q \\ \theta \end{bmatrix} + \begin{bmatrix} X_{\delta_e} & X_n \\ Z_{\delta_e} & Z_n \\ M_{\delta_e} & M_n \\ 0 & 0 \end{bmatrix} \begin{bmatrix} \delta_e(t-\tau_{\delta_e}) \\ n(t-\tau_n) \end{bmatrix} \tag{4}$$

where u is the x-axis body velocity, θ is the pitch angle, and n is the motor rotational speed. U_0, W_0, and Θ_0 are the trim x- and z-axis body velocities and trim pitch angle, and g is the gravity constant. The X, Z, and M terms are the longitudinal dimensional stability and control derivatives to be identified.

The state space model in Eq. (4) models the short-period and phugoid dynamics of the UAS. For certain applications, such as flight simulation, it is important to model both longitudinal modes. Often, the LSS derivatives, X_u, Z_u, and M_u, cannot be identified from frequency domain data, and separate modeling approaches are needed. In our previous work [3], the short-period mode was accurately identified, but LSS derivatives were either dropped from the model structure or identified with high variance. In this paper, trim data was used to determine these derivatives. Additionally, the phugoid mode dynamics are identified from oscillation time-history data to further validate the frequency domain results.

B. UAS Platform

The system identification procedure was performed using the KHawk Zephyr3-R UAS, which was developed by the Cooperative Unmanned Systems Laboratory (CUSL) at the University of Kansas. Vehicle specifications are shown in Table 1, and the UAS is pictured in Fig. 2. The Zephyr3-R is a flying-wing UAS with two elevons and an electric brushless motor as control inputs. The elevons are controlled by mixing the aileron and elevator commands generated by a human pilot or autopilot via Eqs. (5-6), where a positive value indicates deflection of the trailing edge downward. The elevons are actuated by Spektrum A5040 mini digital servos.

$$\delta_{\text{left}} = 0.5(\delta_e^c + \delta_a^c) \tag{5}$$

$$\delta_{\text{right}} = 0.5(\delta_e^c - \delta_a^c) \tag{6}$$

Table 1 KHawk Zephyr3-R UAS specifications.

Mass (kg)	Wingspan (cm)	Cruise Speed (m/s)	Mean Aerodynamic Chord (cm)	Wing Area (m^2)
2.18	122	15-17	31	0.413

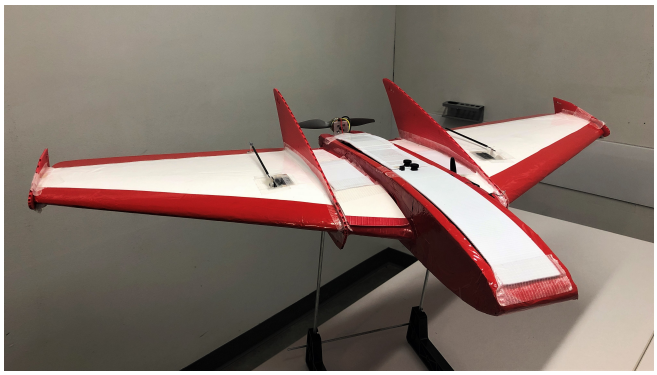

Fig. 2 KHawk Zephyr3-R UAS.

The propulsion system consists of an AXI 2814/10 brushless motor, a Castle Phoenix Edge 75 electronic speed controller (ESC), and an APC 8x4e propeller. The propulsion system is powered by 3-cell lithium-polymer batteries (nominal voltage = 11.1 V). The UAS is equipped with a Hex Cube Pixhawk autopilot running ArduPilot open-source firmware that is used for sensing, control, telemetry, and data logging. Inertial measurement unit (IMU) and command signal data were recorded at 100 Hz by the autopilot, and the motor RPM was recorded at 10 Hz by the ESC.

III. Experiment Design

A. Servo Model Identification

The servo dynamics were identified by measuring the deflection angle of the elevon during ground-tests. A Microstrain 3DM-GX3-25 IMU was fixed to the elevon surface with tape and used to record the deflection angle, as shown in Fig. 3. The deflection angle is estimated from an onboard extended Kalman filter (EKF). The consistency of this filter was verified by comparing the estimates with integrated gyroscope measurements. The IMU weighs 28g and the elevon weighs 40g. This additional weight may affect the dynamics, which should be addressed in future experiments. Experiments were repeated with the IMU mounted on top and beneath the elevon in attempt to average out any errors caused by the mounting of the IMU.

Frequency sweep signals were generated in the aileron and elevator channels of the autopilot. The command signals were normalized to have a range of ±1. The signal frequency increased exponentially from 0.1 to 7 Hz over 60 seconds with a magnitude of ±20% (corresponding to ±3° deflection), which is a typical operating range during flight tests. A frequency response was generated from the measured deflection and command signal, and a first-order transfer function of the form in Eq. (1) was identified to fit the measured frequency response. Time delay was not identified as the measurements had to be synchronized manually. Instead, this delay is lumped into the later state space model identification results.

Frequency response generation and model fitting was performed using CIFER® [1], which identifies model parameters through minimization of a weighted quadratic cost function representing the magnitude and phase error between the measured and modeled frequency response. Parameter identification results are shown in 2, and the measured and modeled frequency response magnitudes are pictured in Fig. 4. Aileron and elevator deflection angles are defined as half the difference and half the sum of the left and right elevon deflection angles, respectively. The identified models are nearly identical, as is expected based on the elevon mixing equations, and match the measured frequency responses very well, as indicated by the cost function value.

Fig. 3 Elevon deflection angle measurement.

Table 2 Servo model parameters.

Command	$K_{\delta_{e,a}}$	τ_{srv}	Cost	Bandwidth (rad/s)
Aileron	0.235	0.032	4.4	31.2
Elevator	0.236	0.032	3.5	31.2

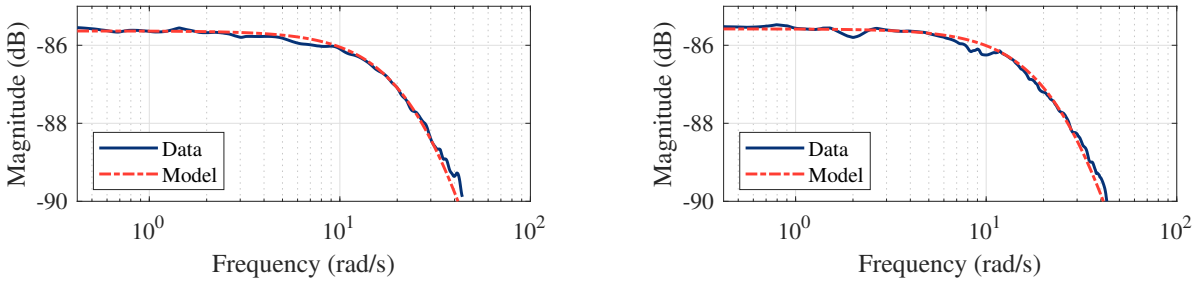

(a) Aileron command-to-deflection model.

(b) Elevator command-to-deflection model.

Fig. 4 Identified servo models.

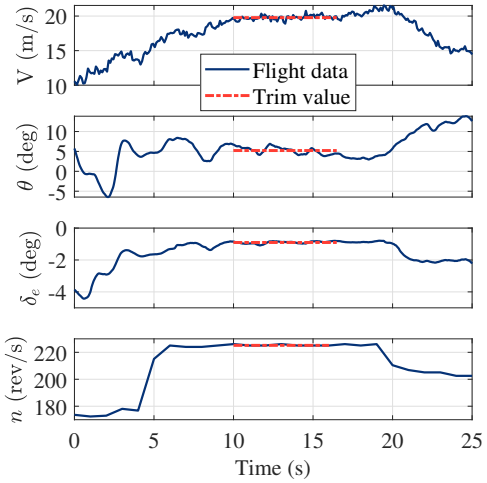

Fig. 5 Example longitudinal speed stability data.

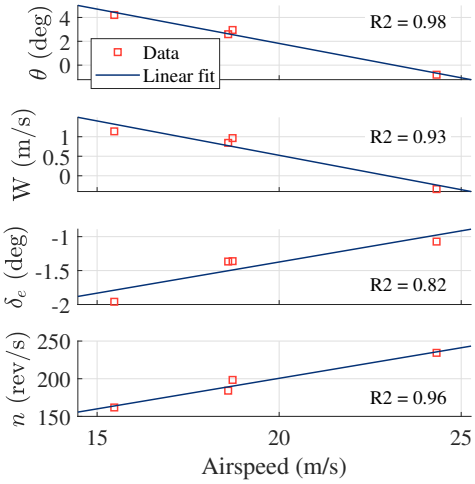

Fig. 6 Trim gradients determined from LSS data.

B. Collection of Longitudinal Speed Stability Data

It is often difficult to achieve accurate identification of the phugoid dynamics from frequency domain data. For small UAS, this can be caused by poor excitation of low frequencies as a result of practical limits on the maximum record time associated with visual line-of-sight flight. This can lead to poor accuracy of the identified LSS derivatives, X_u, Z_u, and M_u. To account for this, derivatives can be determined from trim data [1, 9], hereby referred to as LSS data.

Collecting long periods of trim data can be difficult for small UAS due to their increased susceptibility to atmospheric disturbances. To account for this, steady state data was collected in ArduPilot's "Fly-by-Wire-A" flight mode, which is an attitude-command-attitude-hold control mode. The pilot controlled the throttle manually and stabilized the UAS at different airspeeds. The pitch angle command was also set by the pilot to ensure a near-zero rate of climb or descent. Once the UAS was stabilized, data was collected for about 10 seconds and the mean pitch angle, airspeed, motor speed, and elevator command were taken as the trim values. One set of LSS data is shown in Fig. 5.

The LSS data is used to determine a linear relationship between the measured data and airspeed. Linear trim gradients are fit to the data, shown in Fig. 6, and used in conjunction with the identified state space parameters to identify the LSS derivatives. The LSS derivatives are computed from Eq. (4), evaluated at steady state ($\Delta\dot{x} = 0$) [1]. For example,

$$\Delta\dot{u} = X_u\Delta u + X_w\Delta w - g\cos\Theta_0\Delta\theta + X_{\delta_e}\Delta\delta_e + X_n n = 0 \tag{7}$$

$$X_u = -X_w\left(\frac{\Delta w}{\Delta u}\right) + g\cos\Theta_0\left(\frac{\Delta\theta}{\Delta u}\right) - X_{\delta_e}\left(\frac{\Delta\delta_e}{\Delta u}\right) - X_n\left(\frac{\Delta n}{\Delta u}\right) \tag{8}$$

and similarly for Z_u and M_u, where Δ indicates the fitted gradient with respect to different trim conditions.

Because the identified state space parameters are required for computation, this is an iterative process. The LSS derivatives should be fixed, then the state space parameters identified, then the LSS derivatives should be recomputed, and this should be repeated until the results converge. This process is preferred to identifying the speed derivatives from frequency responses, as low enough frequencies are not typically measured to provide accurate results, which may lead to errors in the derivatives [1, 9]. For example, Z_u may be identified with a positive sign, which corresponds to a negative steady state lift coefficient for low-speed UAS flight (see Sec. IV.D).

C. System Identification Maneuvers

An important step of system identification flight test planning is the design of the input excitation signal. For frequency response measurement, input signals should excite the aircraft response uniformly over a desired range of frequencies. In this paper, automated frequency sweep inputs are used. Key parameters for input design include the frequency range, signal magnitude, and record length. For a UAS, these parameters may need to be adjusted for each day or even each flight based on the atmospheric conditions [3].

First, automated elevator frequency sweeps were designed to excite the short-period dynamics. The sweeps were programmed into the autopilot with configurable parameters that could be modified in real-time based on observations of the UAS response. The sweep ranged in frequency from 0.5 to 7 Hz over a period of 23 seconds. UAS time-history data during an elevator sweep is shown in Fig. 7. Note that the maximum sweep frequency is above the bandwidth of the servos, reiterating the importance of accurately identifying and accounting for the servo dynamics. The flight test procedure for the elevator sweeps is discussed in further detail in [3].

Throttle sweeps were performed manually by the UAS pilot. A toggle-able throttle curve was programmed into a Spektrum DX9 remote control transmitter to limit the pulse-width modulation (PWM) inputs corresponding to minimum and maximum stick deflection. The curve was programmed such that the stick midpoint was the trim throttle setting, and minimum and maximum stick deflections corresponded to ±10% from the trim setting. During the flight test, the pilot would enable the programmed curve only for throttle system identification maneuvers. Before maneuvers, the pilot would communicate with the ground station operator to ensure the current aircraft state was near the desired trim state (e.g., airspeed). During maneuvers, flight data was monitored via real-time telemetry and information regarding the quality of maneuver, such as airspeed or signal-to-noise ratio, was relayed to the pilot. These steps ensured that satisfactory data was collected, and the addition of the programmable throttle curve reduced pilot workload, allowing for more efficient data collection.

An example throttle maneuver is shown in Fig. 8. Due to scheduling constraints, the data was collected on a gusty day, which limited the maneuver length and required the pilot to make active corrective inputs to stabilize the UAS during flight maneuvers. However, these inputs are not strongly correlated with the throttle sweep, as seen in the figure. Additionally, most of the data was collected at an average airspeed 18% higher than the airspeed for elevator sweep data, which can be disadvantageous for identification. Despite this, the maneuvers provided good excitation of the speed dynamics and ultimately resulted in accurate identification results.

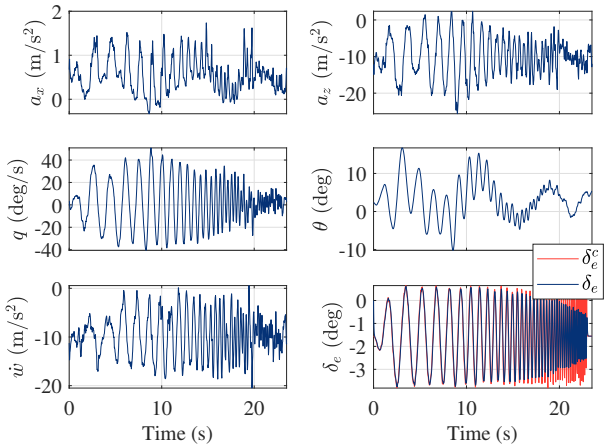

Fig. 7 Time-history of elevator sweep maneuver.

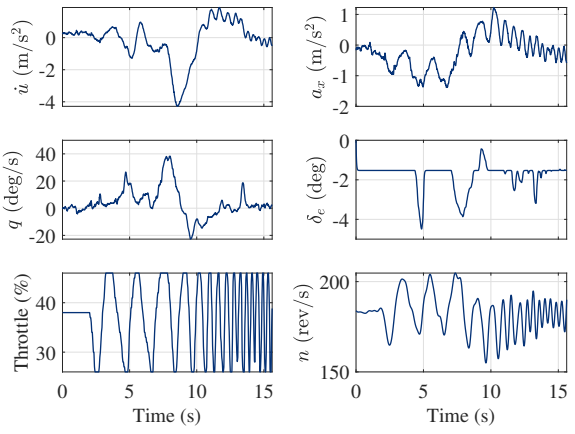

Fig. 8 Time-history of throttle sweep maneuver.

IV. Identification Results

This section outlines the main system identification results. Flight data was processed, synchronized, then used to generate frequency response data. Parameters of the linear longitudinal state space model in Eq. (4) were identified to fit the frequency responses using CIFER®. The parameters identified from LSS data were fixed during the state space identification process. The identified model fully characterizes the short-period and phugoid modes. The phugoid mode is also identified from oscillation time-history data to further validate the identified model. Finally, nondimensional stability and control derivatives and their confidence intervals were computed from the identified model.

A. Data Processing

Prior to using the data for model identification, several pre-processing steps were performed to ensure satisfactory data quality, particularly concerning the motor speed measurements. Due to limitations with the existing hardware, the motor RPM had to be recorded separately on the ESC and at a lower sample rate (10 Hz). Additionally, the identified servo model was used to estimate the elevon deflection from the aileron and elevator command signals.

Data recorded on the ESC was initially synchronized to the Pixhawk data based on the throttle PWM signals recorded by each device. However, analysis revealed a delay between the throttle PWM signals recorded by the ESC and Pixhawk. If the data was aligned by these two measurements, the UAS response would lead the RPM signal, indicating improper synchronization. To avoid this, the RPM measurement was synchronized to the Pixhawk throttle signal. Thus, it is assumed that, at steady state, the motor responds instantly to the Pixhawk throttle signal. Because of this, identified phase and time delays represent the summation of the motor speed-to-UAS response delay and the Pixhawk-to-ESC throttle signal delay. Future experiments will be devoted to separate the individual effects of each of these delays. Finally, the RPM data was interpolated to 100 Hz using sinc interpolation [2].

B. Longitudinal State Space Model

Frequency responses were generated to model the UAS response to elevator and motor speed inputs. Five longitudinal responses to the elevator and two responses to motor speed were used for model identification. State space model parameters were estimated to minimize the error between the modeled and measured frequency responses at frequencies with high coherence. The measured and modeled frequency responses are plotted in Fig. 9. Each model fits well with the measured response, as indicated by the low individual cost functions ($J < 50$ is typically seen as a very good fit [1]). The response to motor speed was identified over a relatively narrow band, which could be improved in the future if longer flight data records are collected.

The identified dynamic modes and state space model parameters are listed in Table 3 and 4. Compared to our previous work, the phugoid mode is now fully identified. All identified parameters are shown to have high accuracy as indicated by the Cramér-Rao bounds and insensitivities, which are all below or near recommended values ($\overline{\text{CR}} \leq 20\%, \bar{\text{I}} \leq 10\%$ [1]). The parameters Z_q, X_{δ_e} and M_n were removed from the model structure because of large insensitivity values, indicating that these parameters have a negligible effect on the UAS dynamics. The identified motor speed time delay is inflated because of the low sample rate and synchronization process discussed earlier.

The identified state space model was verified against time domain flight data. A sample pitch doublet and throttle step maneuver are shown in Fig. 10 and 11. The model accurately predicts the response to both control inputs. The Theil inequality coefficient (TIC), which represents the normalized root mean square error between the model and data, is 0.10 and 0.18 for the two maneuvers. Values below 0.25 generally indicate high accuracy [12].

Table 3 Identified longitudinal dynamic modes.

Dynamic Mode	Poles	Damping Coefficient	Natural frequency (rad/s)
Short-period	-6.55 ± 5.91j	0.74	8.82
Phugoid	-0.102 ± 0.803j	0.13	0.809

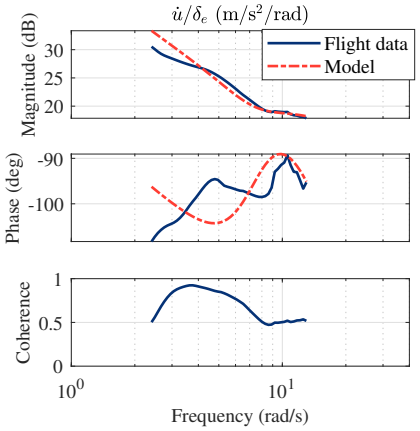

(a) Elevator to x-axis body velocity derivative, $\dot{u}/\delta_e$, model fit (J = 29.9).

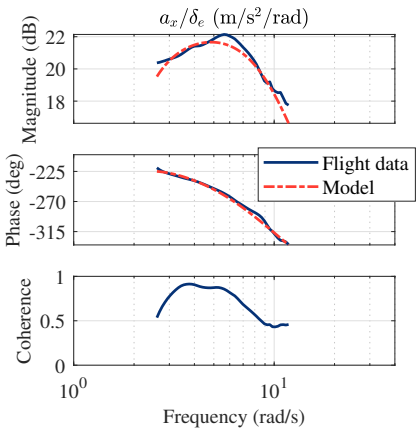

(b) Elevator to longitudinal acceleration, a_x/δ_e, model fit (J = 3.6)

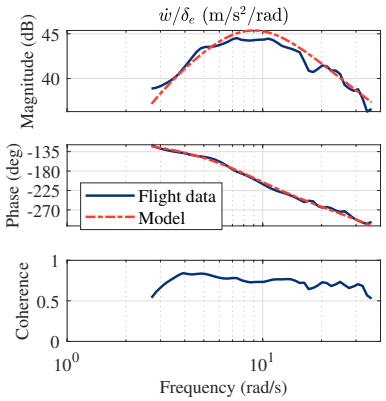

(c) Elevator to z-axis body velocity derivative, $\dot{w}/\delta_e$, model fit (J = 10.5).

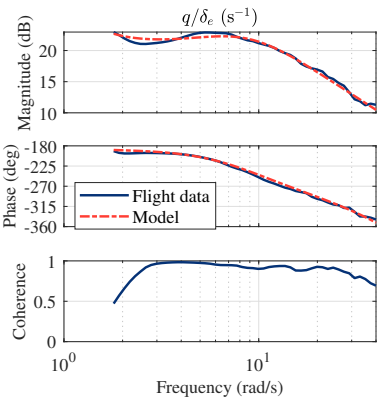

(d) Elevator to pitch rate, q/δ_e, model fit (J = 7.7).

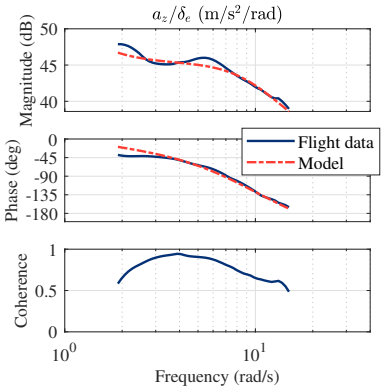

(e) Elevator to vertical acceleration, a_z/δ_e, model fit (J = 20.4).

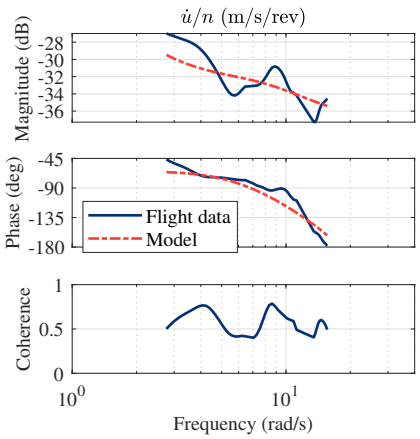

(f) Motor speed to x-axis body velocity derivative, $\dot{u}/n$, model fit (J = 55.9).

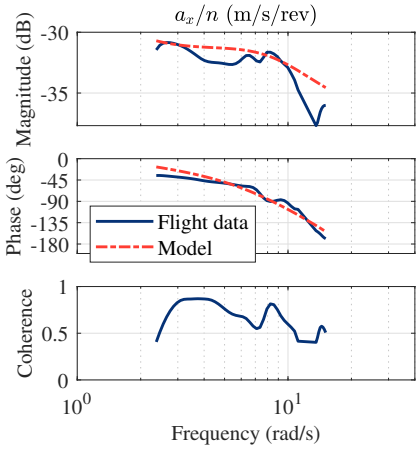

(g) Motor speed to longitudinal acceleration, a_x/n, model fit (J = 35.5).

Fig. 9 Longitudinal state space model fit (J = 23.4).

Table 4 Longitudinal state space model parameters.

Parameter	Unit	Value	Cramér-Rao Bound (%)	Insensitivity (%)
X_u*	s^{-1}	-0.1090	-	-
X_w	s^{-1}	0.5500	7.4	1.3
X_q	m/s	-0.3182	22.7	5.2
Z_u*	s^{-1}	-3.045	-	-
Z_w	s^{-1}	-6.805	5.3	1.5
M_u*	$(m \cdot s)^{-1}$	-0.1464	-	-
M_w	$(m \cdot s)^{-1}$	-2.041	11.0	2.7
M_q	s^{-1}	-6.395	12.7	1.7
X_n	m/(rev·s)	0.01321	17.5	3.2
Z_{δ_e}	m/s^2	-30.26	22.0	7.3
Z_n	m/(rev·s)	0.2270	16.8	3.1
M_{δ_e}	rad/s^2	-132.9	5.3	1.0
τ_{δ_e}	s	0.0398	6.2	2.5
τ_n	s	0.1507	6.7	1.7

*Speed derivatives determined from LSS method and fixed during identification

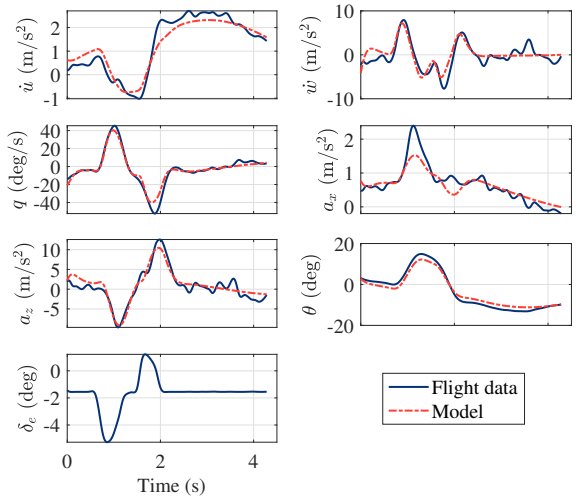

Fig. 10 Pitch doublet time domain validation results (TIC = 0.10).

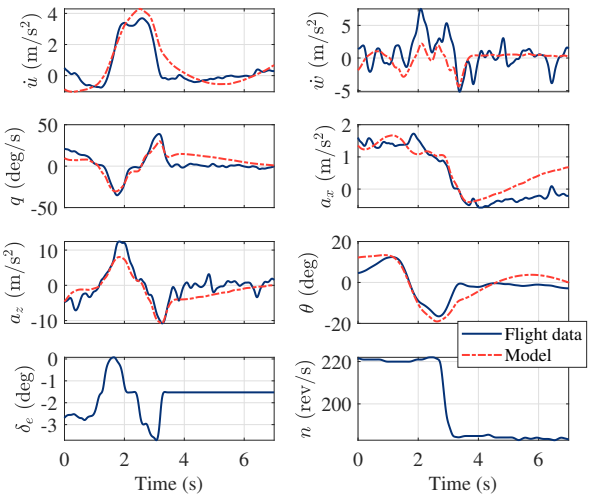

Fig. 11 Throttle step time domain validation results (TIC = 0.18).

C. Phugoid Mode Time Domain Identification

The phugoid mode dynamics were also identified in the time domain to verify the results from the state space model identification. Flight data was collected with the longitudinal controls fixed (small roll corrections were made to maintain stability), and phugoid dynamics were measured from the oscillations observed in the ground speed and pitch angle. As with system identification maneuvers, collecting long periods of data with no longitudinal stick inputs is difficult for small UAS, which constrained the maximum data length to 15 to 25 seconds. Despite this, accurate phugoid mode identification results were achieved with low variance and good agreement with the identified state space model.

Phugoid oscillation time-history data is shown in Fig. 12. The data was processed with a low-pass filter to reveal smooth peaks in the oscillation. A linear trendline was fit to the data, and the time between peaks, T, and the difference between the peaks and the trendline, z, were measured. Then, the damping ratio, damped natural frequency, and undamped natural frequency were calculated using the logarithmic decrement method for underdamped systems [13].

$$\zeta = \frac{\ln(z_1/z_0)}{\sqrt{\ln(z_1/z_0)^2 + 4\pi^2}} \tag{9}$$

$$\omega_d = \frac{2\pi}{T_{12}} \tag{10}$$

$$\omega_n = \frac{\omega_d}{\sqrt{1-\zeta^2}} \tag{11}$$

Seven peak-to-peak oscillations were measured and averaged to determine the phugoid dynamics. The time domain- and frequency domain-identified phugoid mode parameters are compared in Table 5. The 2σ value is shown in parentheses for the time domain results. The natural frequencies show excellent agreement with each other, indicated by very low percent errors. The time domain-identified damping coefficient has higher variance, but still shows good agreement with the frequency domain result. All frequency domain results are within the 2σ bound of the time domain results.

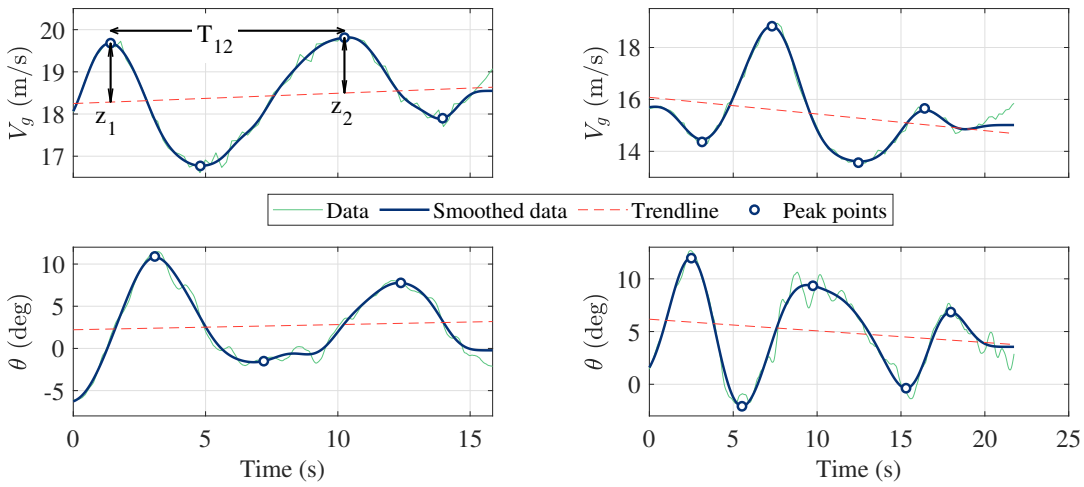

Fig. 12 Phugoid oscillation data.

Table 5 Comparison of phugoid mode identification results.

	Frequency Domain	Time Domain	Percent Error (%)
Damped Natural Frequency (rad/s)	0.755	0.719 (±0.075)	4.8
Undamped Natural Frequency (rad/s)	0.809	0.759 (±0.074)	6.2
Damping Coefficient	0.13	0.10 (±0.08)	23

D. Nondimensional Stability and Control Derivatives

Nondimensional stability and control derivatives were computed from the identified state space model parameters. This form of the derivatives can provide useful physical insight and a means for comparison with other modeling methods, such as wind tunnel test results or CFD simulation [14].

The nondimensional stability and control derivatives were computed using equations from [15]. This calculation is a combination of multiple variables that each have their own associated uncertainty, including the dimensional derivatives, steady state conditions (which are particularly uncertain for a small UAS), and moment of inertia terms, which were measured using the compound pendulum method [16]. Because of this, uncertainty levels were estimated from Monte Carlo style simulation. State space parameters and other variables, such as trim conditions and inertial properties, were sampled as Gaussian random variables and used to iteratively compute the nondimensional derivatives and their uncertainty until the probability distribution converged, as described in [3].

The dimensional LSS derivatives, X_u, Z_u, M_u, are direct functions of the steady state lift, drag, and pitching moment coefficients. In the stability axis coordinate system, the LSS derivatives are computed as [15]

$$\begin{aligned} X_u &= \frac{\rho S U_0}{m}(-C_D^* - C_{D_u}) \\ Z_u &= \frac{\rho S U_0}{m}(-C_L^* - C_{L_u}) \\ M_u &= \frac{\rho S U_0 c}{I_y}(C_m^* + C_{m_u}) \end{aligned} \tag{12}$$

where C_D^*, C_L^*, C_m^* are the steady state drag, lift, and pitching moment coefficients, and

$$\begin{aligned} C_{D_u} &= \frac{U}{2}\frac{\partial C_D}{\partial u} \\ C_{L_u} &= \frac{U}{2}\frac{\partial C_L}{\partial u} \\ C_{m_u} &= \frac{U}{2}\frac{\partial C_m}{\partial u} \end{aligned} \tag{13}$$

We assume that C_{L_u} and C_{D_u} are negligible for low-speed flight and that there is no thrust-induced pitching moment, thus, the steady state pitching moment, C_m^*, is also zero. With these assumptions, we have an equal number of equations and unknown variables, and thus can solve for all nondimensional stability and control derivatives. The identified derivatives and uncertainty bounds are plotted in Fig. 13 and listed in Table 6.

Using LSS data to identify the speed stability derivatives directly correlates to estimation of the steady state lift and drag coefficients. If these derivatives are identified from typical frequency response data, they may result in errors such as a negative steady state lift coefficient. Furthermore, accurately identifying and accounting for the servo dynamics ensures that the nondimensional derivatives represent the bare-airframe and do not include servo effects. This is critical for accurate comparison with other modeling methods such as wind tunnel tests or CFD simulations. Analysis revealed a 20-25% difference in several derivatives between the bare-airframe and integrated servo-airframe models and, specifically, a 60% difference in C_{m_q}.

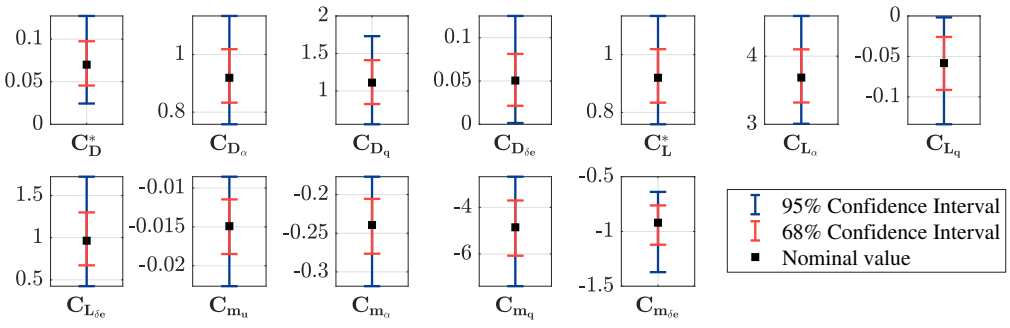

Fig. 13 Longitudinal nondimensional stability and control derivatives.

Table 6 Longitudinal nondimensional stability and control derivatives.

Parameter	Lower Bound (95% Confidence)	Lower Bound (68% Confidence)	Nominal Value	Upper Bound (68% Confidence)	Upper Bound (95% Confidence)
$\mathbf{C_D^*}$	0.0244	0.0455	0.07	0.0975	0.1272
$\mathbf{C_{D_\alpha}}$	0.7578	0.8329	0.9194	1.0187	1.1342
$\mathbf{C_{D_q}}$	0.5567	0.8266	1.112	1.4108	1.7306
$\mathbf{C_{D_{\delta e}}}$	0.0015	0.0214	0.0505	0.0813	0.1251
$\mathbf{C_L^*}$	0.7589	0.8338	0.9201	1.0192	1.1342
$\mathbf{C_{L_\alpha}}$	3.0075	3.3195	3.6854	4.0999	4.5902
$\mathbf{C_{L_q}}$	-0.1339	-0.0914	-0.0583	-0.0259	-0.0018
$\mathbf{C_{L_{\delta e}}}$	0.425	0.6719	0.9642	1.2994	1.7226
$\mathbf{C_{m_u}}$	-0.0226	-0.0185	-0.0149	-0.0115	-0.0085
$\mathbf{C_{m_\alpha}}$	-0.3185	-0.2765	-0.2393	-0.2055	-0.1768
$\mathbf{C_{m_q}}$	-7.3803	-6.0728	-4.8554	-3.7055	-2.686
$\mathbf{C_{m_{\delta e}}}$	-1.3719	-1.1212	-0.92	-0.7622	-0.6388

V. Conclusion

In this paper, several methods were developed and applied to improve longitudinal model identification results for a small, flying-wing UAS. Servo dynamics were identified and used to estimate the real control surface deflection based on elevator commands, which ensured the identified model represented solely the bare-airframe dynamics, rather than the integrated servo-airframe system. This is particularly important for small UAS which often are equipped with low-bandwidth servos. A flight test procedure was developed to collect trim data that was used to identify the LSS derivatives. This LSS data was collected with active feedback control to address the challenge of flying small UAS in open-loop with sticks fixed for long periods. Open-loop elevator and throttle maneuvers were performed to excite the UAS longitudinal dynamics and generate frequency responses used for system identification. A multi-input, multi-output state space model was identified from the frequency responses and fixed LSS derivatives. The frequency response cost function, parameter identification metrics, and time domain verification demonstrated the accuracy of the model. The obtained model was further verified by identifying the phugoid mode dynamics from time domain oscillation data, with both results showing good agreement. Finally, nondimensional stability and control derivatives and their confidence intervals were computed from the identified model. By accounting for servo dynamics during the identification process, the computed nondimensional derivatives represent the bare-airframe rather than the servo-airframe system and should correspond with other modeling methods.

Future work may include performing throttle maneuvers that have a longer record time to better identify low frequency dynamics. This could be achieved through an automated procedure. Additionally, bench tests may be performed to further analyze the effects of individual hardware on system time delays and validate the presented results. In-flight sensing of control surface position can provide more accurate control deflection measurement used for system identification. Finally, motor dynamics models can be identified, which may be useful for applications such as autopilot design or flight simulation.

Acknowledgements

This work is supported in part by the USDA-NIFA Grant 2019-67021-28992, the Army Research Lab Grant W911NF-22-2-027, and the University of Kansas School of Engineering Research and Innovation Seed (RISe) Funding.

References

[1] Tischler, M., and Remple, R., *Aircraft and Rotorcraft System Identification: Engineering Methods with Flight-test Examples*, AIAA, Reston, VA, 2006.

[2] Klein, V., and Morelli, E., *Aircraft System Identification: Theory and Practice*, AIAA, Reston, VA, 2006.

[3] Matt, J. J., Hagerott, S. G., Svoboda, B. C., Chao, H., and Flanagan, H. P., "Frequency Domain System Identification of a Small Flying-Wing UAS," *AIAA SCITECH Forum*, 2022. https://doi.org/10.2514/6.2022-2407.

[4] Dorobantu, A., Murch, A., Mettler, B., and Balas, G., "System Identification for Small, Low-Cost, Fixed-Wing Unmanned Aircraft," *Journal of Aircraft*, Vol. 50, No. 4, 2013, pp. 1117–1130. https://doi.org/10.2514/1.C032065.

[5] Woodrow, P., Tischler, M., Mendoza, G., Hagerott, S. G., and Hunter, J., "Low Cost Flight-Test Platform to Demonstrate Flight Dynamics Concepts using Frequency-Domain System Identification Methods," *AIAA Atmospheric Flight Mechanics (AFM) Conference*, 2013. https://doi.org/10.2514/6.2013-4739.

[6] Flanagan, H. P., Hagerott, S. G., and Chao, H., "Model Based Roll Controller Tuning and Analysis for Small UAS in Turbulent Environments," *2018 International Conference on Unmanned Aircraft Systems (ICUAS)*, 2018, pp. 1398–1407. https://doi.org/10.1109/ICUAS.2018.8453442.

[7] Sanders, F. C., Tischler, M., Berger, T., Berrios, M. G., and Gong, A., "System Identification and Multi-Objective Longitudinal Control Law Design for a Small Fixed-Wing UAV," *2018 AIAA Atmospheric Flight Mechanics Conference*, 2018. https://doi.org/10.2514/6.2018-0296.

[8] Babcock, J. T., Osteroos, R. K., and Tischler, M. B., "Open and Closed Loop System Identification of the Stryker 200 UAV," *AIAA SCITECH 2022 Forum*, 2022. https://doi.org/10.2514/6.2022-2405.

[9] Berger, T., Tischler, M. B., Hagerott, S. G., Christopher Cotting, M., and Gray, W. R., "Identification of a Full-Envelope Learjet-25 Simulation Model Using a Stitching Architecture," *Journal of Guidance, Control, and Dynamics*, Vol. 43, No. 11, 2020, pp. 2091–2111. https://doi.org/10.2514/1.G005094.

[10] Brandt, J., Deters, R., Ananda, G., Dantsker, O., and Selig, M., "UIUC Propeller Database, Vol. 1-3," https://m-selig.ae.illinois.edu/props/propDB.html, retrieved May 2022.

[11] Simmons, B. M., Gresham, J. L., and Woolsey, C. A., "Aero-Propulsive Modeling for Propeller Aircraft Using Flight Data," *Journal of Aircraft*, Vol. 0, No. 0, 0, pp. 1–16. https://doi.org/10.2514/1.C036773.

[12] Jategaonkar, R. V., *Flight Vehicle System Identification: A Time Domain Methodology*, AIAA, Reston, VA, 2006.

[13] Iman, D. J., *Engineering Vibration*, Pearson Education, Inc., Upper Saddle, NJ, 2008.

[14] Rahmani, S., Wang, Z., Matt, J. J., Lin, Z., Chao, H., Zheng, Z., Keshmiri, S., and Ewing, M., "Comparison of Low- and High-Fidelity CFD Based Estimates of Forces, Moments, and Aerodynamic Coefficients with UAS Flight Test Data," *AIAA AVIATION Forum*, 2022. https://doi.org/10.2514/6.2022-4065.

[15] McRuer, D., Ashkenas, I., and Graham, D., *Aircraft Dynamics and Automatic Control*, Princeton University Press, 1973.

[16] Gracey, W., "The Experimental Determination of the Moments of Inertia of Airplanes by a Simplified Compound-Pendulum Method," *NACA-TN-1629*, 1948.